# Electro-optic probe measurements of electric fields in plasmas

# Electro-optic probe measurements of electric fields in plasmas

(iD) **M. Nishiura, Z. Yoshida, T. Mushiake, et al.**

View Online          Export Citation          CrossMark

## ARTICLES YOU MAY BE INTERESTED IN

# Electro-optic probe measurements of electric fields in plasmas

M. Nishiura,[1,a)] Z. Yoshida,[1] T. Mushiake,[1] Y. Kawazura,[1] R. Osawa,[2] K. Fujinami,[2] Y. Yano,[1] H. Saitoh,[1] M. Yamasaki,[1] A. Kashyap,[1] N. Takahashi,[1] M. Nakatsuka,[1] and A. Fukuyama[3]

[1]*Graduate School of Frontier Sciences, The University of Tokyo, Chiba 277-8561, Japan*
[2]*SEIKOH GIKEN Co., Ltd., Matsudo, Chiba 270-2214, Japan*
[3]*Department of Nuclear Engineering, Kyoto University, Nishikyo-ku, Kyoto 615-8540, Japan*

The direct measurements of high-frequency electric fields in a plasma bring about significant advances in the physics and engineering of various waves. We have developed an electro-optic sensor system based on the Pockels effect. Since the signal is transmitted through an optical fiber, the system has high tolerance for electromagnetic noises. To demonstrate its applicability to plasma experiments, we report the first result of measurement of the ion-cyclotron wave excited in the RT-1 magnetosphere device. This study compares the results of experimental field measurements with simulation results of electric fields in plasmas. *Published by AIP Publishing.* [http://dx.doi.org/10.1063/1.4974740]

## I. INTRODUCTION

Ion cyclotron range of frequencies (ICRF) wave heating is an attractive ion-heating method in fusion plasma ignition. For efficient ion heating, researchers have investigated the excitation, propagation, and absorption of radio frequency (RF) waves in plasmas as wave physics since early stage[1] in linear, tokamak, helical, and other fusion devices. The different magnetic structures of these devices characterize the inherent propagations and absorptions of waves. The intensities and phases of RF magnetic fields have been extensively detected by magnetic probes; consequently, the dispersion relation of excited waves has been elucidated.[2,3] By measuring the magnetic fields in plasmas, we can characterize the excited ion cyclotron waves in plasmas.[4]

We considered that direct measurements of RF electric fields will improve our physical understanding of wave propagation and absorption in plasmas, leading to an efficient ICRF heating approach for fusion plasma devices. Electro-optic (EO) sensors based on the Pockels effect are widely used in communications,[5] ion thrusters,[6] and electromagnetic compatibility measurements.[7] In the EO sensor system, the sensor head is electrically separated from the signal acquisition circuit. Therefore, the EO system should minimize the disturbance of the wave fields and reduce the intense mixing with environmental noise.

Section II of this paper develops the EO sensor system and demonstrates its ability to measure electric fields in the magnetosphere plasmas of the Ring Trap 1 (RT-1) device, which is used in advanced fusion researches. However, the vacuum vessel of the RT-1 device and the experimental room during the discharges are inevitably subjected to strong stray fields induced by electron cyclotron (EC) heating and ICRF heating. Under these conditions,

the EO system that uses an optical transmission is superior to the conventional magnetic probe in measuring the wave fields in terms of the high tolerance for electromagnetic noises.

The RT-1 device is based on the dipole field concept and was motivated by spacecraft observations in the Jovian magnetosphere.[9] This magnetic structure for plasma confinement, first proposed by Hasegawa,[10] was built as the RT-1 device at the University of Tokyo.[11] Another such device is the Levitated Dipole Experiment (LDX) constructed at MIT.[12] To produce a laboratory magnetosphere, the RT-1 device uses a klystron and a magnetron operating at 8.2 GHz and 2.45 GHz, respectively, for EC heating and to generate a high electron beta plasma ($\beta_e > 1$).[13,14] Although the RT-1 device reports the anisotropic state of ions in the high electron beta state,[15] the ion beta remains low. In order to achieve a high ion-beta state, we have studied ICRF heating in the magnetosphere configuration.[16] The antenna excites a slow wave with left-handed polarization (slow L wave) at a frequency of a few MHz. The electromagnetic wave propagates along the magnetic fields from the high to low field sides. This so-called *magnetic beach* heating[1] has been studied in various machines.[2–4,8,16,17] In demonstrations, this ion heating scheme was confirmed to increase the ion temperature.

The wave physics of ICRF heating in the magnetosphere dipole configuration remains unclear. Because conventional linear machines differ in their magnetic field structures, the possible propagation of the excited waves is carefully considered to access the absorption area. Magnetic field direction and strength, and electron densities and temperatures limit the propagation and absorption of waves. Conventionally, electromagnetic waves excited in plasmas are characterized by the wave magnetic fields detected by magnetic probes. The merits of this method are local measurement, cost effectiveness, and high heat endurance. However, the electrostatic components, for example, potential oscillations by the antenna voltage, electrostatic waves, and unexpected mode converted waves, are not detectable. RF electric fields are evaluated by a finite

a)Electronic mail: nishiura@ppl.k.u-tokyo.ac.jp

element method based on cold plasma theory, namely, the TASK/WF2 code[18] developed for tokamaks, and by the linear machine Gamma-10.[9] The TASK/WF2 code was applied in the first study of magnetosphere configuration.[16] The present paper is restricted to electric field measurements in plasmas by the EO probe.

Section III presents the RT-1 device and its related accessories. The measured electric field profiles in air and plasmas are compared with simulation results. In these tests, the antenna excites a MHz wave. The results extend the predictive accuracy of the simulation and enhance our understanding of the physical processes. Furthermore, plasmas may be affected by phenomena derived from antenna potential oscillations and electrostatic wave excitations, which are not detectable by conventional magnetic probes. The results are comprehensively discussed in Section IV, and a concluding summary is presented in Section V.

## II. ELECTRO OPTIC PROBE FOR ELECTRIC FIELD MEASUREMENTS

Two types of electric field probes based on the Pockels effect have been developed; the interferometer (IF)-type EO-sensor[7] and the bulk-crystal-type EO-sensor.[5] The former is equipped with an optical waveguide containing a miniature antenna on $LiNiO_3$ substrate, and the latter detects the change in polarization angle caused by a change in the refractive index. This paper employs the EO sensor (CS-1403, SEIKOH GIKEN Co., Ltd., Japan). Figure 1 shows a schematic of the EO sensor system and the details of the sensor head on the $LiNiO_3$ crystal substrate. The single-mode optical-fiber (SM fibers) is spliced onto the optical waveguide fabricated on the substrate. The sensor head is enclosed in an acrylic resin case of volume

$(6 \times 5.5 \times 23.5)$ mm$^3$ for shock protection. The EO sensor detects electric field intensities from 1 V/m to 25 kV/m and frequencies from 100 kHz to 10 GHz. The bottom part of Fig. 1 depicts the measurement setup of the electric field. Polarized light from a laser source with a wavelength and power of 1.55 $\mu$m and 16 dBm, respectively (CoBrite DX1, ID Photonics, Germany), is delivered to the EO sensor (denoted as Pockels in Fig. 1) via polarization-maintaining optical fibers (PM fibers) and a circulator. Single-mode optical fibers (SM fibers) connect the EO sensor to an InGaS PIN photo detector (Newport, wavelength 1000–1650 nm, bandwidth 12.5 GHz). The laser light is divided into two optical waveguides fabricated into the $LiNbO_3$ crystal substrate. This optical waveguide system forms the interferometer that amplitude-modulates the optical signal. The laser light passing through one optical waveguide acquires the electric field generated by a printed dipole antenna on the $LiNbO_3$. The electric field changes the refractive index of the $LiNbO_3$, causing a phase delay of the laser light. The phase of the laser light through the other waveguide is unchanged. Both laser lights are reflected at the end mirror of the EO sensor and are merged into one beam on the $LiNbO_3$. The interfered signal passes through the circulator and is measured by the InGaS PIN photo detector. The output signal of the photo detector is monitored by a spectrum analyzer (Anritsu, MS2720T, bandwidth 9 kHz–20 GHz) with a time resolution of 100 ms. The EO sensor head mounted on RT-1 is electrically separated by a 21-m long SM fiber (measured from the sensor head). The remaining components are placed at the control room to reduce the electromagnetic noises. The EO sensor was directed transversely to the optical fiber axis.

For electric field measurements in RT-1, the sensor head was encapsulated inside a quartz tube of diameter 24 mm,
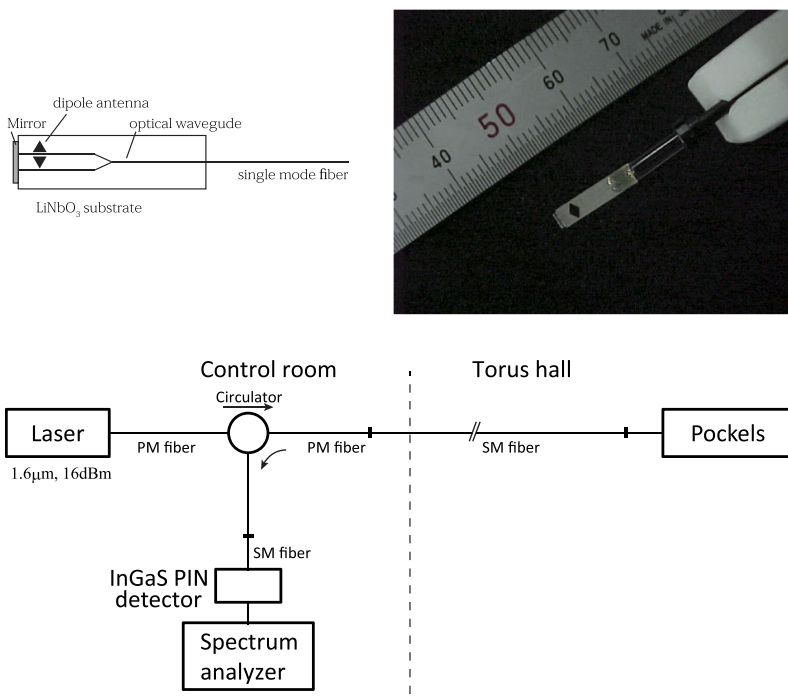


FIG. 1. Measurement setup of electric field with the EO sensor. Upper left shows the internal structure of the EO sensor tip. Upper right is a photograph of the EO sensor. The acrylic resin case, which normally protects the tip from shock, has been dismounted for the photograph.
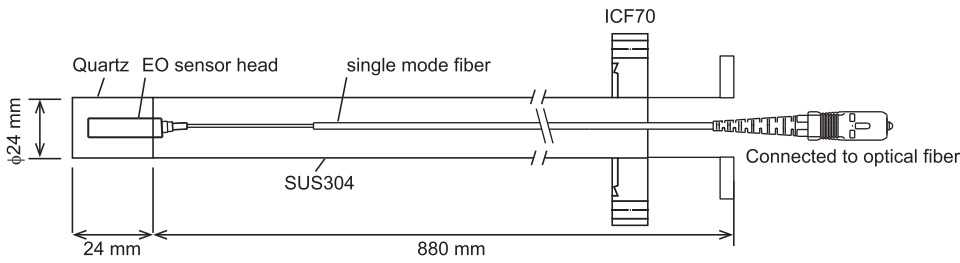
FIG. 2. Schematic of the EO sensor mounted in a shaft for inserting into RT-1 plasmas. To measure the spatial profile, the shaft is mounted on a motor drive system at the flange.

thickness 5 mm, and length 24 mm, as shown in Fig. 2. The quartz tube was closely contacted to a stainless steel tube (SUS304) and vacuum-sealed by a Viton O-ring. The tube interior was filled with air. The optical fiber from the EO sensor head was led to the outside of the stainless steel tube. As the operating temperature of the EO sensor is limited to below 60 °C, we confirmed prior to measurement that the temperature inside the quartz tube never exceeded 60 °C at the experimental plasma discharge.

Prior to experiments, we also obtained the absolute intensity of the electric fields and the radiation pattern. For this purpose, the EO sensor was characterized in the MHz range. A known electromagnetic wave from a synthesizer was introduced to the shield box and was radiated by an antenna. The electromagnetic absorbers surrounded the inner wall surface. The EO sensor head was placed at the center of the shield box, and the radiation pattern was measured at 3 MHz while rotating the sensor head on the optical fiber axis (see Fig. 3). The directional sensitivity was approximately one order of magnitude higher at 0° and 180° than at 90° and 270°. The radiation pattern acquisition was repeated at 1 and 2 MHz. The calibration factors fluctuated within a few dB up to 10 GHz.
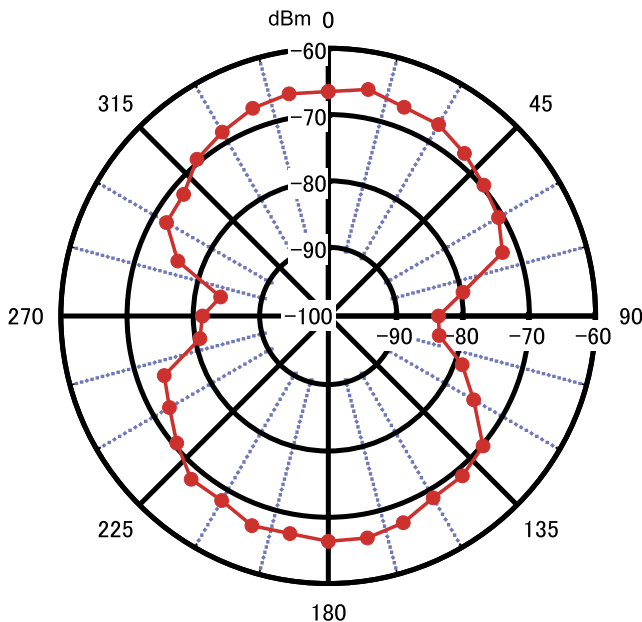
## III. MEASUREMENT OF RF ELECTRIC FIELDS FOR ION HEATING IN MAGNETOSPHERE PLASMAS

Figure 4 shows the top and cross-sectional views of RT-1.[14] To create the dipole field, the superconducting levitation magnet inside the vacuum vessel is levitated by the lifting magnet, which is a normal conductor. The high-temperature superconducting wires of the levitation magnet are composed of Bi-2223. The plasma in this experiment was produced by EC heating while filling with helium gas. The ICRF heating was accomplished by a double-loop antenna mounted on the center stack with supporting rods, which are electrically insulated from the vacuum vessel. For magnetic beach heating, the ICRF wave fields are excited at the lower and upper loop antennas located at $\omega/\Omega_{He^{2+}} \sim 0.58$ and $\omega/\Omega_{H^+} \sim 0.66$, respectively, at the interior high-field side. Figure 5 displays the current directions through the antenna. One end of the antenna is connected to the current feedthrough, which feeds RF power from a RF power supply with a nominal output of 10 kW in the 1–3 MHz range. Reflections are reduced by a matching box placed between the feedthrough and the RF power supply. The other end of the antenna is connected to the grounded vessel.

The EO sensor measures the RF electric fields in RT-1 plasmas. To obtain the vertical profile of the electric field in the theta (toroidal) direction, $E_\theta$, we inserted the EO sensor (enclosed in its supporting rod) from the top port (#5-T-0) of RT-1 at the radial position R = 0.245 m. The EO sensor detected the stray electromagnetic waves radiating from the EC and ICRF heating in the RT-1 vacuum vessel. Panels (a) and (b) of Fig. 6 show typical spectra of the 3-MHz ICRF wave and the EC wave at the nominal frequency of 2.45 GHz during plasma shots. These spectra were acquired by a spectrum analyzer with a time resolution of a few hundred milliseconds. The absolute electric field was obtained by subtracting the noise floor from the peak and multiplying the subtracted value by the calibration factor.

To evaluate the EO sensor system, we compared the measured electric fields in air and plasma with those calculated by the TASK/WF2 code, which solves Maxwell's equations in the cold plasma limit in cylindrical coordinates $(r, z)$ by a finite-element method, assuming toroidal symmetry. The conductor boundaries are the vacuum vessel of RT-1, the levitation coil, and the center stack. Quantitative comparisons require the antenna current, which is measured by a current transformer placed at the current feedthrough close to the antenna. Figure 7 shows the profile of $E_\theta$ at 3 MHz measured at R = 0.245 m. In this case, the antenna was excited at 3 MHz



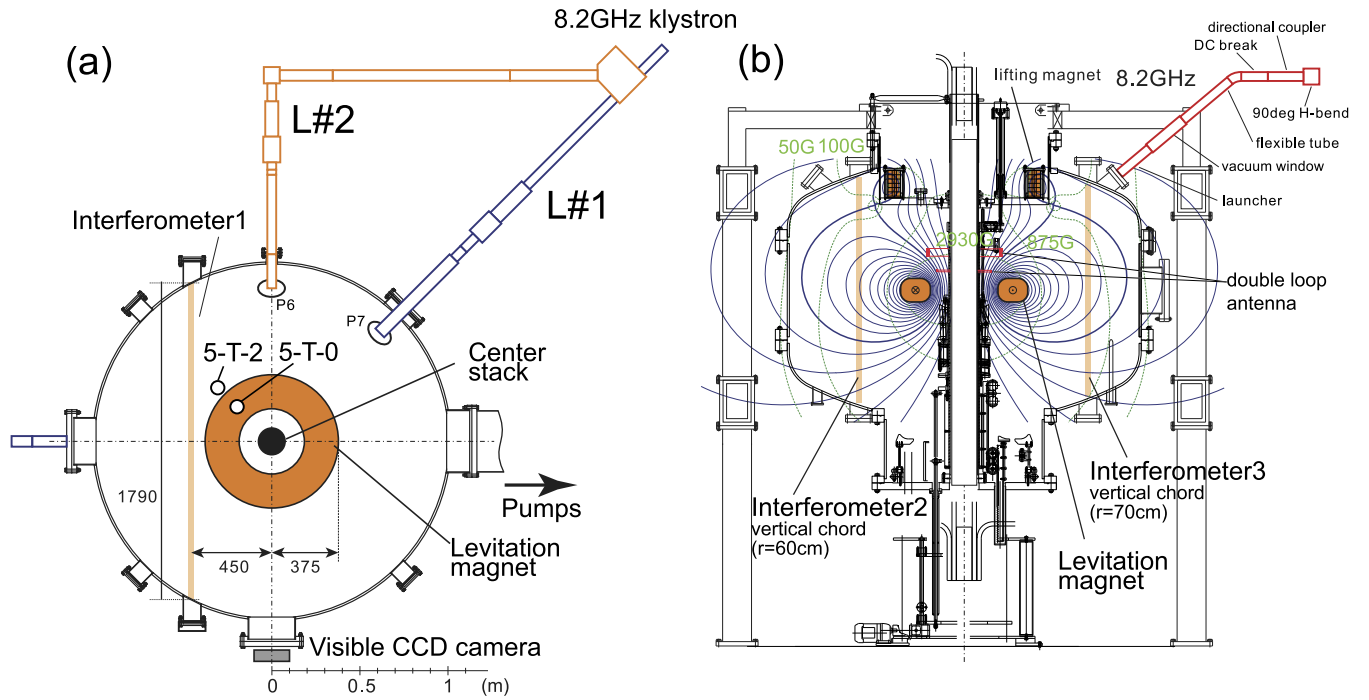FIG. 3. Radiation pattern of the EO sensor acquired at 3 MHz.

FIG. 4. Magnetosphere plasma device RT-1. (a) Top view and (b) cross sectional view. For the electric field measurements, the EO sensor head was inserted from the 5-T-0 (R = 0.245 m) and 5-T-2 (R = 0.72 m) ports. The double-loop antenna for ICRF heating is mounted on the center stack.

and 5 A. This signal level is sufficient for comparisons among the results. The EO sensor was scanned in the Z direction. The EO sensor head contacted the double-loop antenna at $Z = 0.22$ m. The measured $E_\theta$ quantitatively agreed with the simulation, and both methods obtained reliable results. The signal of the EO probe reached the background level at $Z \geq 0.32$ m. Figure 8 shows the EO sensor, the double-loop antenna, and the levitation superconducting magnet in the vacuum vessel. The EO sensor in the ICRF plasma experiments was inserted at $R = 0.72$ m, further than in the air experiments.

The power of the EC heating ($P_{ECH} = 12.2$ kW) sustains the plasma discharge for 1 s at the helium gas pressure of 2.1 mPa. At the onset of the discharge, the ICRF heating initiates electromagnetic wave excitation by the double-loop antenna. The ion heating is accomplished by the *beach heating* method.[1] The excited slow wave propagates parallel to the magnetic field from high to low magnetic-field sides and

is absorbed at the ion cyclotron layer in the lower magnetic fields. With each shot, the EO sensor was vertically moved at $R = 0.72$ m (5-T-2 port in Fig. 4). The temperatures of the He$^+$ and C$^{2+}$ ions were monitored by the Doppler broadening of bulk helium ions (He II, $\lambda = 468.57$ nm) and impurity ions (C III, $\lambda = 464.74$ nm) in the equatorial plane. In the discharge, the radial profiles of the He II and C III ion temperatures peaked at $T_i \sim 10$ eV and $\sim 30$ eV, respectively. The peaks appeared at $R = 0.7$ m in the plane $Z = 0$. The interferometers (IFs) #1 and #3 measured the line-averaged electron densities $\bar{n}_0$ along
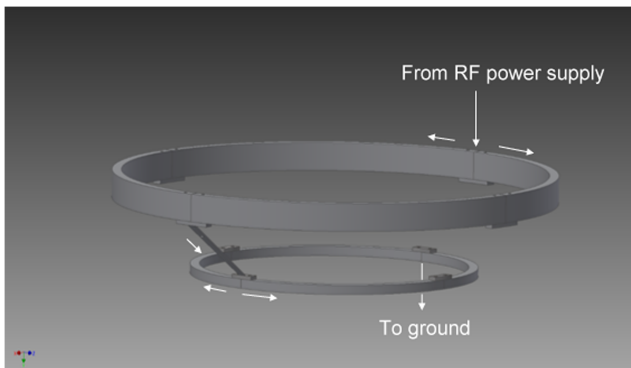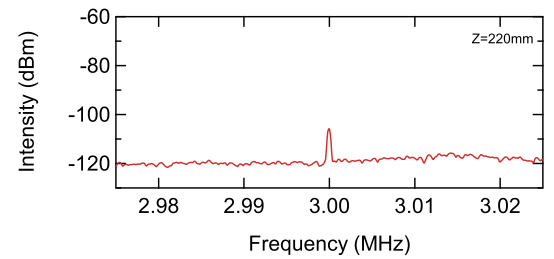


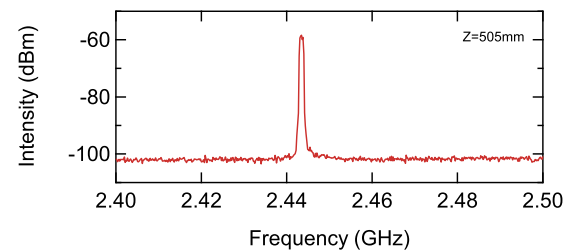(a) Spectrum of ICRF wave measured by the EO sensor



(b) Spectrum of EC wave measured by the EO sensor

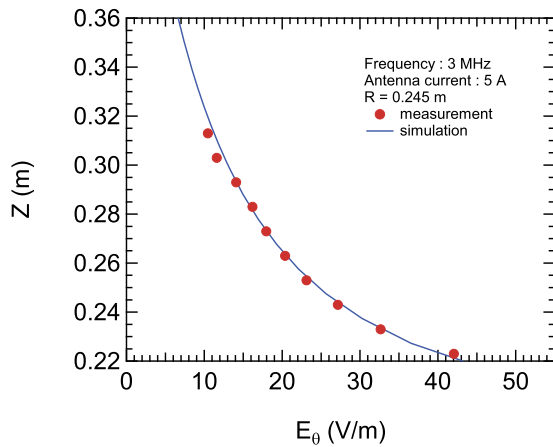FIG. 6. Typical spectra in the (a) MHz and (b) GHz ranges during EC heating discharge.



FIG. 5. Double-loop antenna and RF current flow for ICRF heating in RT-1.

FIG. 7. Electric field profile of $E_\theta$ at 3 MHz measured by the EO sensor (closed circles) in RT-1 in the air experiments. The simulation result (blue curve) is also plotted.
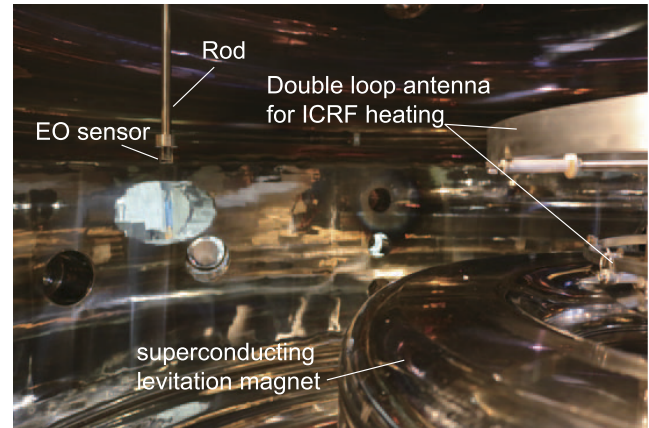


FIG. 8. The EO sensor mounted inside the supporting rod is inserted from the top port. The vacuum vessel of RT-1 contains the levitation superconducting magnet and the double-loop antenna for ICRF heating.

the central chord, where the horizontal line of sight passes through $R = 0.45$ m, and $\bar{n}_{edge}$ along the peripheral chord, where the vertical line of sight passes through $R = 0.6$ and $0.7$ m. The discharge conditions in the figures are summarized in Table I.

To calculate the wave fields, we input the experimental parameters into a TASK/WF2 simulation. For reconstructing the electron density profile, we assumed a flux surface function of $1/R$ in the dipole field of RT-1 and evaluated the line averaged densities of the interferometers. The TASK/WF2 code calculates the excitation by the double-loop antenna, the propagation and the power absorption of waves in plasmas. Figure 9 shows the electric field and the ICRF power-absorption profiles simulated in RT-1. The last closed flux surface (LCFS) is indicated. The power-absorption area of $He^{2+}$ exists on the ion cyclotron layer between the upper and lower antennas. Hence, only the slow L wave excited at the lower antenna achieves the ion cyclotron resonance layer for $He^{2+}$; the upper antenna does not contribute to ion heating. Moreover, no $He^{2+}$ heating occurs at an ICRF frequency of 2 MHz. The simulation suggests that during ICRF heating, the power absorption of the waves increases at lower frequencies (1–4 MHz) and higher electron densities ($10^{15}$–$10^{19}$ m$^{-3}$). These features are consistent with the slow L wave propagation from high to low magnetic fields.

Figure 10 compares the measured and simulated $E_\theta$ values as Z is varied. The measured $E_\theta$ exceeds the simulated $E_\theta$ beyond the LCFS at $Z = 0.35$ m. In contrast, within the plasma confinement region, the field strength of the wave decreases and the results coincide at $Z = 0.3$ m. The discrepancy might arise from the antenna potential oscillation, which was ignored in the TASK/WF2 simulation. In the experiment, the

double-loop antenna oscillated at a few kV under an RF power input of 10 kW. This electrostatic oscillation might deviate the measured and simulation results beyond the confinement region. To suppress spurious wave excitations, a Faraday shield is required for the double-loop antenna.

The electron density profile in front of the antenna might also cause the discrepancy in wave field strength between the simulated and measured results. To verify the edge density profile, we vertically measured the edge electron density $n_{edge}$ at $R = 0.72$ m, replacing the EO probe with a double probe. The edge electron density was smoothly connected to the core plasma across the LCFS at $Z = 0.35$ m. Therefore, the peaked profile of $E_\theta$ observed in Fig. 10 cannot be attributed to the edge density profile.

The RF electric fields along the line $R = 0.72$ m were measured during ICRF heating under different discharge conditions (listed in Table I). The ICRF heating was conducted at 3 MHz. Figure 11 shows the profiles of the RF electric fields in helium plasma at fill gas pressures of 2.1 mPa and 4.4 mPa. The input powers for EC and ICRF heating were almost identical in the two discharges. From core to edge, the electron density was higher at 4.4 mPa than at 2.1 mPa. We surmise that the higher electron density increases the wave absorption efficiency, reducing $E_\theta$ at the EO sensor position. The peak in the $E_\theta$ profile at the LCFS remained at the higher electron density.

The RF electric fields were measured during ICRF heating in helium and in mixed hydrogen–helium plasmas. The results are plotted in Fig. 12. To measure the ion temperature, we introduced a small amount of helium into the hydrogen plasma. The applied frequency was set to 2 MHz. In both cases, the RF electric fields at $Z = 0.35$ m were stronger than at 3 MHz,

TABLE I. Discharge conditions and plasma parameters for generating Figs. 10–12.

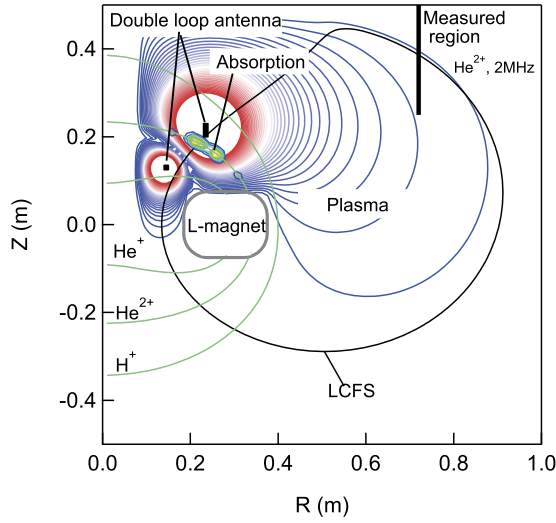| Gas (mPa) | $P_{EC}$ (kW) | $P_{ICRF}$ (kW) | $f_{ICRF}$ (MHz) | $I_{ant}$ (A) | IF#1 (m$^{-3}$) | IF#2 (m$^{-3}$) | IF#3 (m$^{-3}$) | Remarks |
|---|---|---|---|---|---|---|---|---|
| He, 2.1 | 12.2 | 6.8 | 3 | 252 | $1.6 \times 10^{17}$ | $3.0 \times 10^{16}$ | $1.0 \times 10^{16}$ | Red circles in Figs. 10 and 11 |
| He, 4.4 | 12.4 | 7.0 | 3 | 250 | $3.9 \times 10^{17}$ | $7.3 \times 10^{16}$ | $1.5 \times 10^{16}$ | Blue circles in Fig. 11 |
| He, 4.6 | 13 | 9.2 | 2 | 296 | $3.1 \times 10^{17}$ | $5.2 \times 10^{16}$ | $2.4 \times 10^{16}$ | Blue circles in Fig. 12 |
| H 8.0 He 0.6 | 13 | 10 | 2 | 280 | $1.8 \times 10^{17}$ | $4.2 \times 10^{16}$ | $1.8 \times 10^{16}$ | Red circles in Fig. 12 |

FIG. 9.  Contours of the electric field $E_\theta$ excited by the double-loop antenna in helium plasma. L-magnet indicates the levitation magnet. The antennas are located outside the LCFS. The contours of the power absorption area for $He^{2+}$ are also plotted. The ion cyclotron layers for $H^+$, $He^{2+}$, and $He^+$ are depicted.
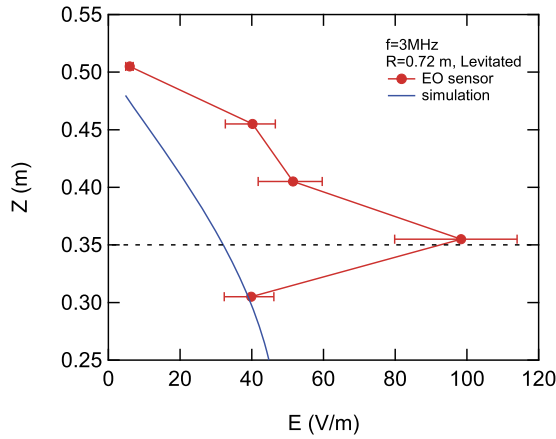


FIG. 10.  $E_\theta$ (closed circles) vertically measured by the EO sensor along $R = 0.72$ m in helium plasma. The ICRF power is 7 kW. The separatrix (dashed line) is located at $(R, Z) = (0.72$ m, $0.35$ m). The input parameter for the simulation was the measured antenna current (252 A).

being measured as 185 V/m in the hydrogen–helium mixture and 95 V/m in the helium plasma. The antenna current at 2 MHz was 280–296 A, 1.2 times higher than at 3 MHz. Therefore, $E_\theta$ was increased by the higher RF input power and electron density. Again, the electric fields were peaked at the LCFS. The local measurement of RF electric fields clarified an unexpected wave excitation during ICRF heating of the magnetosphere plasmas. The EO sensor system is a powerful tool for studying wave physics in plasmas. However, the underlying wave physics and the relation between the observed electric fields and the ion heating efficiency require further careful investigation.

## IV. DISCUSSION ON RF ELECTRIC FIELDS EXCITED IN PLASMAS

$E_\theta$ measured along the Z direction shows a local maximum near the LCFS. The peaked profile of the measured $E_\theta$



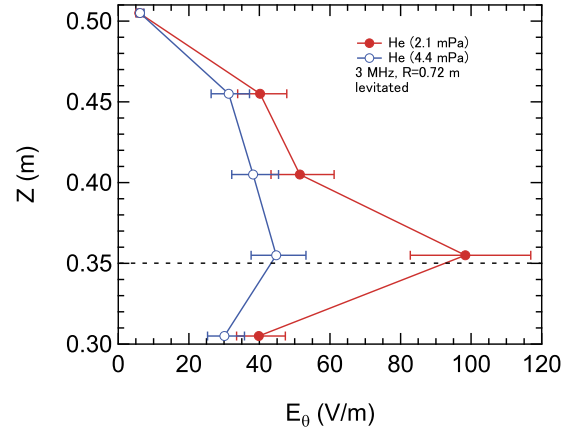FIG. 11.  $E_\theta$ measured by the EO sensor in helium plasmas. The helium gas pressures were 2.1 mPa (closed circles) and 4.4 mPa (open circles).



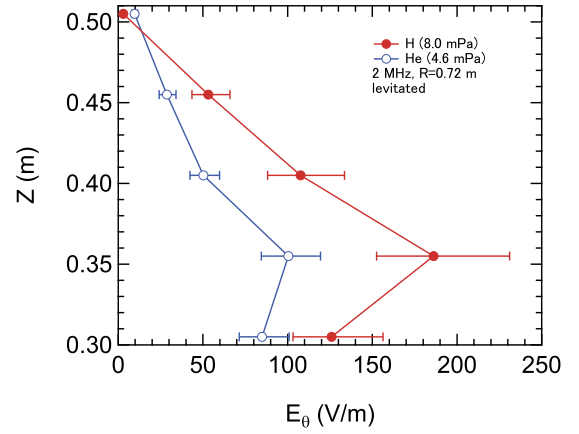FIG. 12.  $E_\theta$ measured by the EO sensor in plasmas. The fill gas pressures are mixed hydrogen at 8.0 mPa and helium at 0.6 mPa (closed circles) and helium at 4.6 mPa (open circles).

in Fig. 10 cannot be replicated by the TASK/WF2 code. We now attempt to interpret the measured $E_\theta$. The signal of the EO probe might cause incomplete separation of $E_\theta$ from the radial and vertical $E$ components ($E_r$ and $E_z$, respectively); however, the measured $E_r$ and $E_z$ components were one order of magnitude lower in sensitivity than $E_\theta$ and were insensitive to the $\theta$ direction.

To evaluate the interference effect in the measured $E_\theta$, we calculated the RF electric fields by the TASK/WF2 code. The main structures of the levitation magnet and the vacuum vessel of RT-1 were entered into the simulation model. The spatial structure was divided into non-structural meshes for the finite element method, and the wave equation of the electric field was given by the Maxwell equation in plasma[18]

$$\nabla \times \nabla \times \tilde{E} + \frac{1}{c^2}\frac{\partial}{\partial t^2}\tilde{E} = -\mu_0 \frac{\partial}{\partial t}\left(\tilde{J} + \tilde{J}_{ext}\right),$$

where $\tilde{J}$ is the perturbed current induced by an RF field and $\tilde{J}_{ext}$ is the external current density. This solution gives the fields and structures of electromagnetic waves in plasmas. The excitation of electromagnetic waves is modeled by feeding $\tilde{J}_{ext}$ to the antenna.
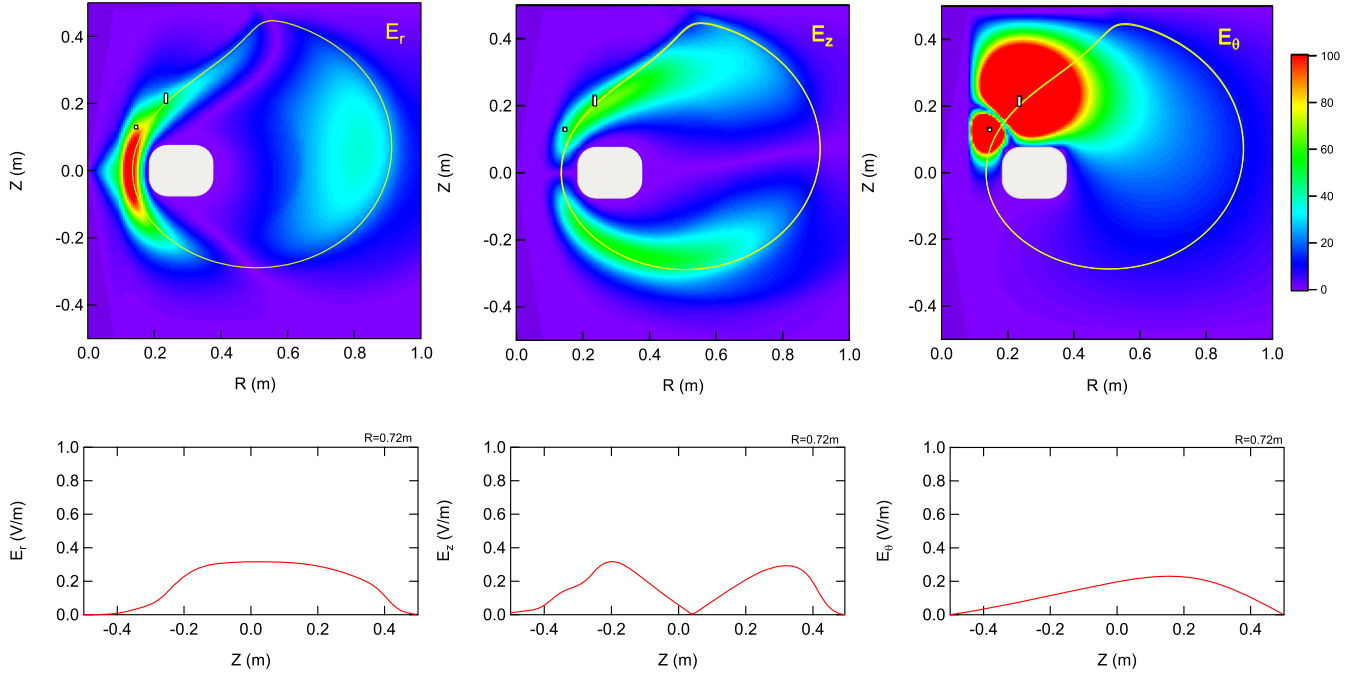
FIG. 13. Two-dimensional profiles of the electric fields excited by the double-loop antenna in RT-1. The current densities in the upper and lower loops are set to $J_{ext} = +252$ A and $-252$ A, respectively. Bottom panels show the profiles of $E_r$, $E_z$, and $E_\theta$ along the line R = 0.72 m in RT-1, plotted from the corresponding 2D profiles.

The sinusoidal antenna potential associated with charged particle fluctuations induces an intense electric field. To simulate this situation, we must modify the TASK/WF2 code. The current density $\tilde{J}_{ext}$ applied to the antenna and its associated electric charge density $\rho_{ext}$ are separated from the plasma-induced terms $\tilde{J}$ and $\rho$. In matrix form, the resulting equation is

$$A \cdot x = b,$$
$$= \begin{pmatrix} \tilde{J} \\ \rho \end{pmatrix} + \begin{pmatrix} \tilde{J}_{ext} \\ \rho_{ext} \end{pmatrix},$$

where the matrix $A$ represents the dielectric constant and permeability in the medium, and $x$ contains the plasma parameters related to densities and temperatures. The electric fields in RT-1 were calculated in two separate cases; $\tilde{J}_{ext}$ with $\rho_{ext} = 0$ that does not take into account for the electrostatic potential of the antenna in plasma and $\tilde{J}_{ext} = 0$ with $\rho_{ext}$ ($\neq 0$) that does take into account for it. We ensured that the result could not explain the peaked $E_\theta$ observed in RT-1. In a toroidal symmetry we expect that the antenna potential cannot excite $E_\theta$. Therefore, in this analysis, we calculated the wave fields in TASK/WF2 with $\tilde{J}_{ext}$ and $\rho_{ext} = 0$.

The two-dimensional profiles of the simulated electric fields in the vacuum vessel of RT-1 are plotted in the upper panels of Fig. 13. The corresponding vertical profiles at $R = 0.72$ m, where the EO probe was scanned, are presented in the lower panels. The double-loop antenna radiates an intense $E_\theta$ in addition to $E_r$ and $E_z$. $E_r$ localizes between the levitation coil and the center post, whereas $E_z$ extends with the LCFS. Caging the antenna by a Faraday shield would effectively avoid the excitation of the local wave fields $E_r$ and $E_z$. Given the directionality of the EO sensor, the interference of $E_r$ and $E_z$ is one order of magnitude lower than the measured $E_\theta$. Therefore, the peaked

$E_\theta$ at the LCFS cannot be explained by interference phenomena and requires further consideration and experimental investigation.

## V. SUMMARY

Employing the EO sensor system, we successfully measured the RF electric fields and analyzed the ICRF heating in laboratory magnetosphere plasmas. RF electric fields excited at 2 and 3 MHz were detected in the 3–200 V/m range at some distance from the double-loop antenna in the plasmas. The TASK/WF2 code, which is based on cold plasma theory, accurately predicted the measured electric fields in air but could not capture the measured $E_\theta$ in plasmas, particularly outside the LCFS. Although the antenna-potential oscillation associated with the antenna excitation failed to resolve the discrepancy between experiment and theory, we suggest that designing the antenna structure and installing a Faraday shield would improve the efficiency of ICRF heating.

## ACKNOWLEDGMENTS

[1] T. H. Stix, *Waves in Plasmas* (American Institute of Physics, New York, 1992), pp. 342–343.
[2] D. R. Roberts and N. Hershkowitz, Phys. Fluids **B4**, 1475 (1992).
[3] A. Ando, M. Inutake, M. Hatanaka, K. Hattori, H. Tobari, and T. Yagi, Phys. Plasmas **13**, 057103 (2006).
[4] J. C. Hosea and R. M. Sinclair, Phys. Fluids **13**, 701 (1970).

[5]H. Togo, A. Sasaki, A. Hirata, and T. Nagatsuma, Int. J. RF Microwave Comput.-Aided Eng. **14**, 290 (2004).

[6]T. Ise, R. Tsukizaki, H. Togo, H. Koizumi, and H. Kuninaka, Rev. Sci. Instrum. **83**, 124702 (2012).

[7]B. Loader, M. Alexander, and R. Osawa, EMC'14/Tokyo 16P3–H1 (2014), http://www.ieice.org/~emc14/.

[8]Y. Yamaguchi, M. Ichimura, T. Ouchi, I. Kozawa, H. Muro, S. Sato, A. Fukuyama, H. Hojo, M. Katano, Y. Motegi, J. Ohishi, T. Murakami, Y. Sekihara, and T. Imai, Fusion Sci. Technol. **55**(2T), 106–109 (2009).

[9]S. M. Krimigis, T. P. Armstrong, W. I. Axford, C. O. Bostrom, C. Y. Fan, G. Gloeckler, L. J. Lanzerotti, E. P. Keath, R. D. Zwickl, J. F. Carbary, and D. C. Hamilton, Science **206**, 977 (1979).

[10]A. Hasegawa, L. Chen, and M. E. Mauel, Nucl. Fusion **30**, 2405 (1990).

[11]Z. Yoshida *et al.*, Phys. Rev. Lett. **104**, 2405 (2010).

[12]A. C. Boxer, R. Bergmann, J. L. Ellsworth, D. T. Garnier, J. Kesner, M. E. Mauel, and P. Woskov, Nat. Phys. **6**, 207 (2010).

[13]H. Saitoh, Z. Yoshida, J. Morikawa, Y. Yano, T. Mizushima, Y. Ogawa, M. Furukawa, Y. Kawai, K. Harima, Y. Kawazura, K. Kaneko, K. Tadachi, S. Emoto, M. Kobayashi, T. Sugiura, and G. Vogel, Nucl. Fusion **51**, 063034 (2011).

[14]M. Nishiura, Z. Yoshida, H. Saitoh, Y. Yano, Y. Kawazura, T. Nogami, M. Yamasaki, T. Mushiake, and A. Kashyap, Nucl. Fusion **55**, 053019 (2015).

[15]Y. Kawazura, Z. Yoshida, M. Nishiura, H. Saitoh, Y. Yano, T. Nogami , N. Sato, M. Yamasaki, A. Kashyap, and T. Mushiake, Phys. Plasmas **22**, 112503 (2015).

[16]M. Nishiura, Z. Yoshida, Y. Yano, Y. Kawazura, T. Mushiake, H. Saitoh, M. Yamasaki, A. Kashyap, N. Takahashi, M. Nakatsuka, Y. Takase, and A. Fukuyama, Plasma Fusion Res. **11**, 2402054 (2016).

[17]T. Watari, K. Adati, T. Aoki, S. Hidekuma, K. Hattori, S. Hiroe, M. Ichimura, T. Kawamoto, R. Kumazawa, Y. Okubo, S. Okamura, T. Sato, C. M. Singh, and M. Sugawara, Nucl. Fusion **22**, 1359 (1982).

[18]A. Fukuyama, K. Itoh, and S.-I. Itoh, Comput. Phys. Rep. **4**, 137 (1986).